crystals

MDPI

Article

Effects of Depth of Cutting on Damage Interferences during Double Scratching on Single Crystal SiC

Duan Nian

Institute of Mechanical Engineering and Automation, HuaQiao University, Fujian 361021, China; duannian@hqu.edu.cn

Received: 27 May 2020; Accepted: 16 June 2020; Published: 17 June 2020

Abstract: In this work, the damage interference during scratching of single crystal silicon carbide (SiC) by two cone-shaped diamond grits was experimentally investigated and numerically analyzed by coupling the finite element method (FEM) and smoothed particle hydrodynamics (SPH), to reveal the interference mechanisms during the micron-scale removal of SiC at variable Z-axis spacing along the depth of cutting (DOC) direction. The simulation results were well verified by the scratching experiments. The damage interference mechanism of SiC during double scratching at micron-scale was found to be closely related to the material removal modes, and can be basically divided into three stages at different DOCs: combined interference of plastic and brittle removal in the case of less than 5 μm, interference of cracks propagation when DOC was increased to 5 μm, and weakened interference stage during the fracture of SiC in the case of greater than 5 μm. Hence, DOC was found to play a determinant role in the damage interference of scratched SiC by influencing the material removal mode. When SiC was removed in a combined brittle-plastic mode, the damage interference occurred mainly along the DOC direction; when SiC was removed in a brittle manner, the interference was mainly along the width of cutting; and more importantly, once the fragment of SiC was initiated, the interference was weakened and the effect on the actual material removal depth also reduces. Results obtained in this work are believed to have essential implications for the optimization of SiC wafer planarization process that is becoming increasingly important for the fabrication of modern electronic devices.

Keywords: damage interference; material removal mode; double scratching; SPH method

1. Introduction

Owing to its superior physical properties such as wide bandgap, high thermal conductivity, and critical breakdown electric field [1–3], single crystal silicon carbide (SiC) has became an ideal wafer material for next-generation microelectronic and photoelectronic devices [4–6], which necessitates a damage free surface and subsurface quality of SiC wafers. However, SiC is hard and brittle and prone to fracture [7–9], and grinding remains to be the most common, if not irreplaceable, technology to planarize SiC substrates for successive polishing. It is well known that the grinding process involves the scratching of workpiece by a large number of abrasive grits with irregular geometries, and sometimes randomly distributed on a grinding wheel. Thus, knowledge of of the damage interference at the surface/subsurface of ground SiC during the scratching by multiple abrasive grits is essential for the advance of wafer planariziation techniques, which cannot be achieved through a simple superposition of the scratching of each individual grit [10]. Given the complicated deformation behaviors during interfered scratching, experimental studies have been carried out to identify the controlling factors in the damage formation during the grinding process of several ceramics. For instance, the subsurface damage of monolithic ceramics and soda lime glass were found to gradually increase with the increase of scratches cycles [11]. The effects of the normal scratching force and spacing distance on damage

formation were studied during inferred scratching on BK7 glass, and it was found that three types of cracking interaction were observed and resulted in different chipping features during double scratching and the material removal volume during double scratching was strongly dependent on separation distance in brittle scratch mode [12]. Moreover, at a given depth of cut, the propagation of lateral cracks in polycrystalline alumina during double scratching was controlled by the grain size of the diamond abrasive grits; meanwhile, the propagation of transverse cracks was dominated by the grain boundary fracture and the grain shedding in alumina workpiece [13]. Li et. al developed a theoretical model to describe the effects of depth of cutting (DOC) on material removal mechanism of Lu_2O_3 ceramics, by taking single and multiple scratches into account. The friction characteristics, the elastic recovery phenomenon, and the surface topography and subsurface damage mechanism during double and multiple scratches were discussed [14].

However, it must be noted that the damage interference occurred through the entire scratching process, and the experimental research relied mainly on the final deformation behaviors to infer the dynamic deformation, removal, and recovering events, and restrictive assumptions and presumptions were often made. On the other hand, numerical methods such as molecular dynamics are used to simulate the double scratching process, which are able to comprehensively consider the effects of the scratching speed, cutting depth, and crystal orientation on the surface topography after multiple scratches [15]. As long as the appropriate algorithm and material constitutive model are properly adopted, the numerical analysis is promising in terms of revealing the dynamic interference during multiple scratching processes. In particular, thanks to the computational efficiency of the smoothed particle hydrodynamics (SPH) algorithm in simulating the large deformation and discontinuous failure process [16–20] and the easy convergence to the finite element method (FEM) method [21–26], the SPH and FEM coupling algorithm has been successfully applied in previous research to model the dynamic removal event during grinding of single crystal SiC [27]. The damage interference mechanisms in the materials removal process of single crystal SiC scratched by two diamond abrasive grits with different y-axis distances was studied by the coupling SPH and FEM method. The difference in the surface morphology of single crystal SiC during the double scratching process [28] has been found to be closely related to the cutting depth of abrasive grits into the workpiece, which in turn obviously affect the material removal mechanism in the scratching process and surface quality of ground SiC [29]. However, a comprehensive understanding on the effect of damage interference in the double scratching at direction along the DOC is yet to be achieved.

In this paper, the damage interference in the double scratching process of diamond abrasive grits was investigated, both experimentally and numerically, to reveal the effects of Z-axis spacings along the DOC direction, in which case the damage interference is the combined action of the effects of the two diamond grits. It has been found that the material removal mechanism of single crystal SiC scratched by diamond abrasive grit was strongly dependent on the DOC, and consequently, the damage interference during double scratching was affected by the material removal modes at variable DOCs in the double scratching process. In addition, after the occurrence of damage interference, the interference behaviors in different material removal modes was completely inconsistent; once the fragment appears, the damage interference effect gradually weakens.

2. Experimentation

2.1. Scratching

To explore the damage interference mechanism in the double scratching process, the scratching experiment was carried out on a BLOHM Planomat HP408 high precision surface grinder (Schleifring, Hamburg, Germany). Scratching experiment was conducted using a stainless-steel grinding wheel in a diameter of 290 mm.When machining the grinding wheel, special attention was given to ensure the perpendicularity of the grinding surface, as well as the axis of the screw hole, to the axis of the inner hole of the wheel. A conical diamond tip with the cone angle of 91.8°, and the tip radius of 40.7 μm

was used to scratch SiC. Figure 1 is a three-dimensional contour view of the tool recorded by a Hirox KH-8700 three-dimensional video microscopy system. As shown in Figure 1, the x-axis is defined as the horizontal direction, consistent with the movement direction of the workbench, and the z-axis is defined as the vertical direction, perpendicular to the x-axis, which is along the scratch depth direction. The three screw holes are equally spaced on the machined grinding wheel. A copper spacer having a thickness of 5 µm was used to accurately control the position of diamond tip along the z-axis during double scratch experiment. Double-side polished single crystal 6H SiC (TankeBlue, Beijing, China) with a diameter of 2 inches and a thickness of 5 mm was used as workpiece and the scratching was on the silicon surface. No coolant was added during the experiment.

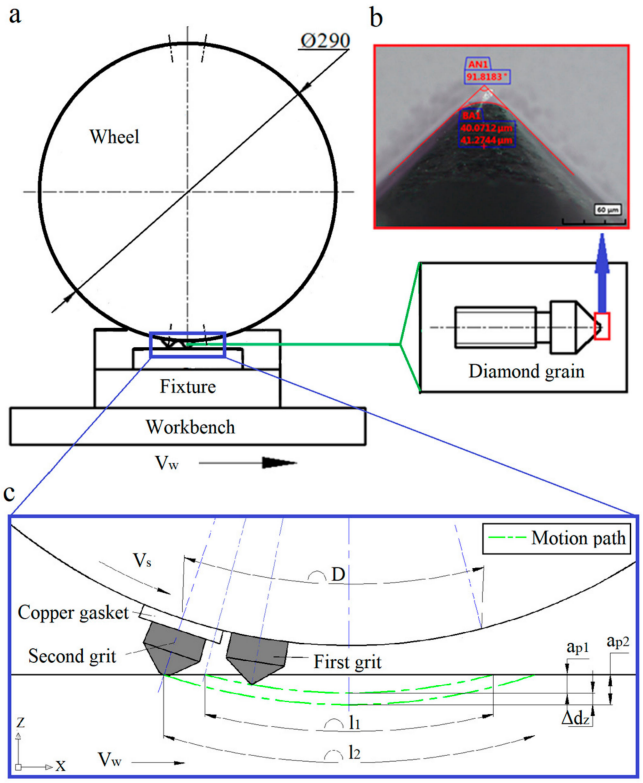

Figure 1. Schematic diagram of twice scratching experimental devices, (**a**) experimental device of two grits scratching, (**b**) detail size of the diamond grain, and (**c**) diagram of interference of twice scratching.

Prior to scratching experiment, the position of diamond tip on grinding wheel was calibrated by standard spacer to an accuracy of the Z-axis spacing along the DOC. Moreover, the parameter of dynamic balance is adjusted to 0.03 g to ensure the dynamic balance during the experiment at a linear speed of 30 m/s. To avoid the influence of the tool tip wear on the scratching result, the diamond tips was replaced after five scratches. The specific experimental parameters in the experiment are shown in Table 1.

Table 1. Experimental parameters of two grits scratching.

Parameter	Value
Velocity of the wheel(v_s)(m/s)	30
Z-axis spacing along the DOC direction (Δd_Z) (µm)	5, 15, 25
Velocity of the workbench (v_w) (mm/min)	20000

2.2. Results

Figure 2a shows the surface morphology of SiC successively scratched by two diamond grits in the Z-axis spacing of 25 microns along the DOC. The contour and related dimensions of the A-A section were detected by a laser scanning confocal system (Zeiss, Oberkochen, German), and hence the actual scratch depth can be reversed by the contact arc length as [30]:

$$l = 2\sqrt{a_p D_s} \tag{1}$$

where l is the contact arc length, a_p is the scratching depth, and D_s is the rotation diameter. According to Equation (1), the scratching depth of second grit is 35.2 μm in Figure 2a, corresponding to less than 1% variation to the setting value of 35 μm. This is because the double scratching experiment was performed after one tool-setting operation, and substantially the scratching depths should be the same. As shown in Figure 2a, a large number of pits appeared on both sides of the scratched groove, with the maximum size of approximately 350 μm in the middle of the groove. The maximum width of the groove is 782 μm, and the maximum depth of the groove is 56 μm.

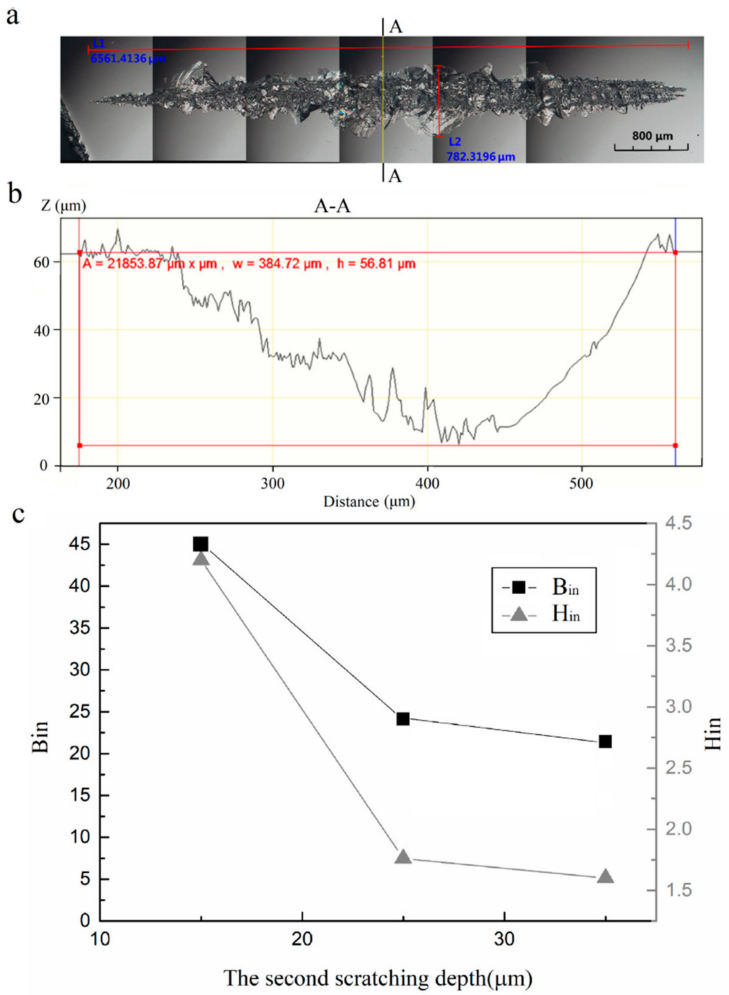

Figure 2. Three-dimension morphology of the groove after scratching by two diamond grain with different Z-axis spacings along the depth of cutting (DOC) direction, (**a**) morphology of the groove Iwith the Δd_z of 25μm, (**b**) profile curve of Section A, and (**c**) *bin* and *hin* of twice scratching with different spacings in Z-axis direction for experiment.

As the scratching depth increased, the maximum value of both the depth and width of the scratched groove was augmented. Therefore, the *bin* and *hin* are used to normalize and evaluate

the degree of interference at variable DOC, as shown in Figure 2b. The *bin* and *hin* are expressed as Equations (2) and (3):

$$hin = \frac{h\max}{ap_2} \tag{2}$$

$$bin = \frac{b\max}{ap_2} \tag{3}$$

where *hmax* is the maximum depth of the groove, *bmax* is the maximum width of the groove, and ap_2 is the scratching depth of the second grit. It can be seen that as the depth of the scratch increased, the values of the corresponding *bin* and *hin* were gradually decreasing. The trend of the *bin* and the *hin* began to decrease rapidly until it approached a threshold value. It is hence reasonable to conclude that the degree of damage interference in brittleness removal firstly decreased rapidly, but eventually reached a stable state. However, the damage interference that occurred in the dynamic double scratching process cannot be directly, and/or in situ, monitored, and the interference mechanism cannot be revealed merely experimentally.

3. Numerical Analysis

To reveal the the interference mechanism at a micron-scale, two models by coupling SPH and FE method [27] with different sizes are developed to simulate double scratching at different Z-axis spacings along the DOC direction. Specifically, the size of the SPH particles and FEM elements of the first model was 25 times larger than the second. The former was used to analyze the interference in the double-scratch process of brittle removal mode when the Z-axis spacings were relatively large, and the later was focused on interference analysis at combined plastic-brittle removal modes when the Z-axis spacings were smaller. In another words, the SPH method was used to model the large plastic deformation and material removal the FEM method was applied to represent the small plastic or elastic deformation, and the coupled FE/SPH algorithm was used to analyse contact coupling area where both plastic and elastic deformation occurs.

3.1. Model Development

To explore the effects of the material removal mode on the damage interference mechanism in the double scratching process, the interference in two grits scratching process was simulated by applying different Z-axis spacings along the DOC at a micron-scale through LSDYNA software (Livermore Software Technology Corporation, California, United States). The micron-scale model was mainly used to represent the damage interference mechanism when materials were in the brittle removal mode and combined plastic-brittle removal mode.

Figure 3 shows the two grits scratching model, where Δd_z stands for the Z-axis spacing along the DOC between the two grits. In the model, these two diamond tips had the same conic geometry. The radius of the bottom circle was 250 μm, the height was 500 μm, the radius of the tip was 40 μm, and the front angle of the grit was −45 degrees (assuming that the grit is a rigid body). As Figure 3 shows, the two diamond grits were set as FE meshes, and the workpiece was divided into three parts: an SPH particle layer which was used to simulate material removal of workpiece, an FE/SPH coupled layer, and an FE mesh layer which was used to simulate small deformation and residual stress of workpiece. The size of the workpiece was 3 mm × 0.5 mm × 0.7 mm. Among them, the size of SPH particles was 3 mm × 0.5 mm × 0.5 mm and the size of each particle was 12.5 μm; the size of FE/SPH coupled layer was 3 mm × 0.5 mm × 0.05 mm; the size of FE mesh was 3 mm × 0.5 mm × 0.25 mm. In the SPH algorithm, the number of particles will greatly affect the calculation accuracy. To more accurately simulate the early stage of damage interference, the size of the double scratch model with a smaller z-axis spacing along the DOC was set to 300 μm × 120 μm × 8 μm. Among them, the size of the SPH part was 300 μm × 120 μm × 6 μm, and the size of each particle was 0.5 μm; the size of the FEM part was 300 μm × 120 μm × 3 μm; and the thickness of the FE/SPH coupling part was 1 μm.

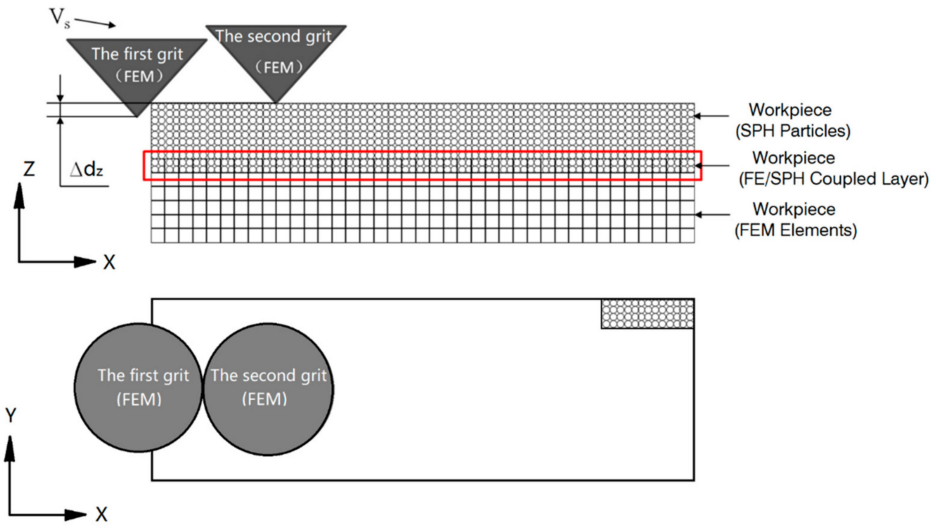

Figure 3. Simulation model of double scratching.

To improve computation efficiency, the following assumptions were made: (1) all physical parameters of single crystal SiC are temperature independent, and (2) the heat conduction of the SiC workpiece is negligible. Moreover, scratching tips were set as is it was a diamond and treated as rigid bodies because of its ultra-high hardness. The parameters of the physical and mechanical properties of single crystal SiC and diamond were adopted from literature data and listed in Table 2. Moreover, the constitutive equation parameters A, B, N, and C, representing the normalized cohesion strength, normalized pressure hardening coefficient, pressure hardening index, and strain rate hardening coefficient in the Johnson–Holmquist–Cook (JHC) model for single crystal SiC, were listed Table 3 [31]. The trajectory of scratching tips was modeled merely along the Y-axis, so the rotational degrees of freedom along the X- and Z-axis and the translation degrees of freedom in the Y-axis direction of the tool were restricted. Full-degree-of-freedom constraints were applied to the bottom of the finite element model. The specific simulation parameters were set to be consistent with the experiments.

Table 2. Physical and mechanical properties of diamond and single crystal SiC.

Material	Density (g/mm^3)	Elastic Modulus (MPa)	Poisson's Ratio
Diamond	3.5e−3	9.64e+5	0.07
Single crystal SiC	3.163e−3	1.83e+5	

Table 3. Johnson–Holmquist–Cook parameters of single crystal SiC.

JHC Parameters	A	B	N	C
Value	0.91	0.085	0.78	0.003

3.2. *Validation*

Figure 4a shows the surface morphology of the SiC scratched by double scratching with a Z-axis spacings of 25 μm. As shown in Figure 4a, a considerable number of pits were distributed on both sides of the scratched groove. Compared with the experimental results, the error of the maximum width and the maximum depth was less than 10%, indicating a reasonable agreement with simulation results. With the increase of the Δd_z, the maximum width of the groove firstly decreased and then increased, and after deducing the corresponding scratching depth of the second grit, the values in the different cases were the same except when Δd_z is 5 μm. These results show that interference is the most obvious when Δd_z is 5 μm. Additionally, the number of cracks in the depth direction increased with the increasing of Z-axis spacing, and the size of the cracks also increased.

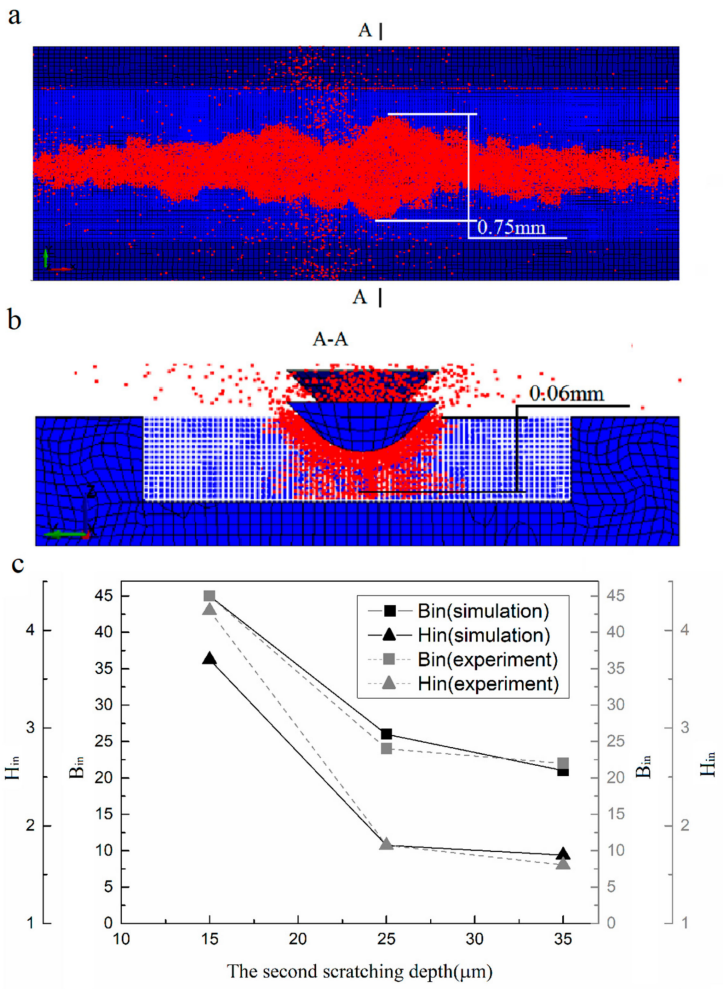

Figure 4. Morphology of the groove after two grit scratching of single crystal SiC with different Z-axis spacings under the brittle removal mode, (**a**) morphology of the groove with the Δd_z of 25 μm, (**b**) material damage in Section A, and (**c**) *bin* and *hin* of twice scratching with different spacings in Z-axis direction for simulation and experiment.

Figure 4b shows the line chart of *bin* and *hin* with different Z-axis spacings along the DOC direction for simulation and experiment. Compared with the experimental results, the trend of the *hin* and *bin* was basically consistent. As can be seen from Figure 4b, the average error between the simulation results and the experimental results was less than 10%, which indicates an effectiveness of FE/SPH algorithm.

Figure 5a shows time history of the material damage interference nephograms during double scratching with the Δd_z of 5 μm. The interference can not be found when t = 0.7 μs. At this time, central and lateral damage induced by the first scratching grit appeared on the surface of the material, while the second grit was not in contact with the material. When t = 2.1 μs, the particles from the material surface after the first scratching were flown out, which indicated that chips were generated. At this time, the second grit was still not in contact with the material, but the lateral damage generated by the first grit had extended to the position at which the second grit was about to contact the material. When t = 2.8 μs, the central damage caused by the second grit scratching and the lateral damage caused by the first grit scratching began to interfere. When t = 4.2 μs, the interference depth reached about 15 μm. When t = 0.0056 ms, due to the close depth of the two grits, massive material damage generated by the two grits had interacted and interfered multiple times. Hence, this led to a further deepening of the maximum removal depth, which was approximately 60 μm. Figure 5b shows scratch interference damage nephograms of the two grits with the Δd_z of 15 μm at different times. When t = 0.7 μs, material

damage of the groove was the same as that when the Z-axis spacing along the DOC direction was 5 μm; when t = 2.1–2.8 μs, the lateral damage caused by the scratching of the second grit and the lateral damage caused by the scratching of the first grit began to interfere. When t = 4.2–5.6 μs, the material removal zone generated by the two grits was completely connected, and the material removal depth reached 45 μm. A second interference between the lateral damage and other derived damage was hardly observed, and the depth of the interference zone was about 25 μm, where the depth of interference zone was the average depth of material damage after interference occurred. Thus, this interference did not affect the maximum material removal depth but had a relatively obvious effect on the maximum width. Figure 5c shows damage interference nephograms of the two grits with the Δd_z of 25 μm at different times. When t = 5.6 μs, the damage of the groove was the same as that for the Z-axis spacings of 5 μm and 15 μm; when t = 1.4–2.1 μs, the lateral damage generated by the second grit interfered with the damage generated by the first grit; and when t = 2.8–5.6 μs, the material removal zone generated by the two grits was completely connected, and the material removal depth reached to 60 μm. However, the depth of the interference zone was still about 25 μm. Therefore, the damage generated by the first grit can hardly affect the maximum depth and width of the groove.

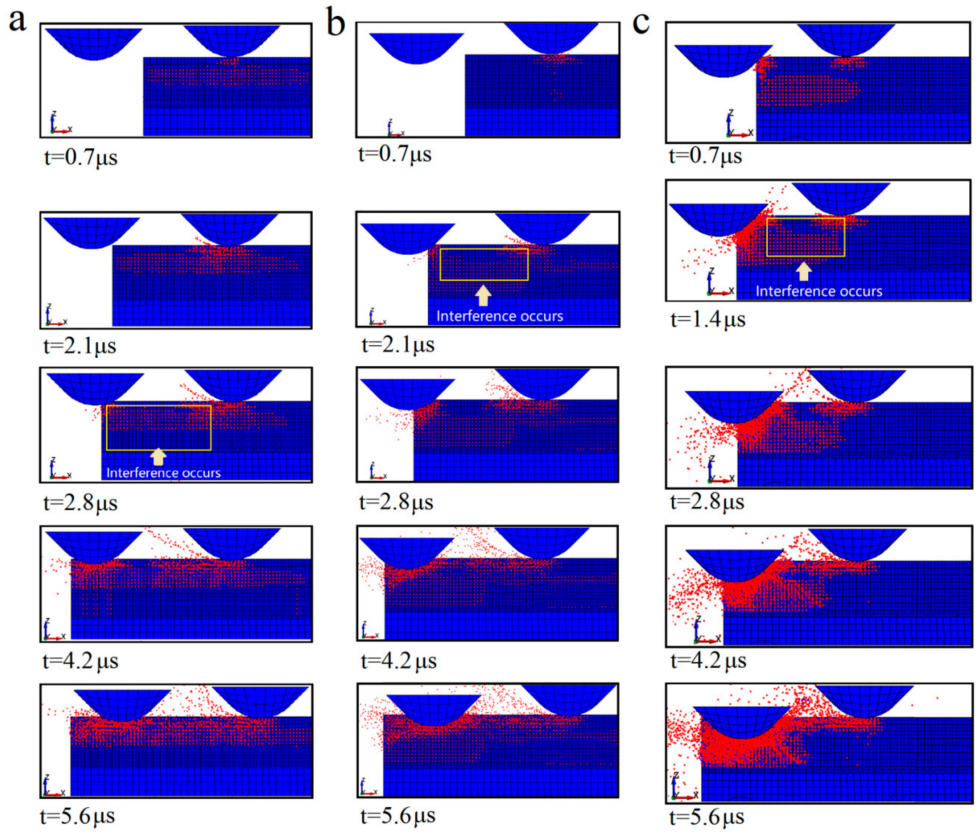

Figure 5. Damage Interference nephograms of two grit scratching of single crystal SiC with a Z-axis spacing along the DOC direction at different times, (**a**) Δd_z is 5 μm, (**b**) Δd_z is 15 μm, and (**c**) Δd_z is 25 μm.

From the above analysis, brittle removal is the main material removal mode in the scratching processes with the Z-axis spacings of 5, 15, and 25 μm along the DOC direction. With the increasing of the Z-axis spacing, the time that interference occurs is continuously advanced. The maximum depth of the groove corresponding to the Δdz of 15μm is the smallest among the three spacings, which is consistent with the experiment results. As far as the interference effect is concerned, it is more obvious when the Δd_z is 5 μm. However, in terms of the effect of material removal depth, as the z-axis spacing

between the two grits along the DOC gradually increases, the influence of interference gradually decreases or even disappears, and the influence of the scratch depth dominates.

4. Discussion

4.1. Damage Interference

To comprehensively analyze the mechanism of damage interference, the simulations of the double-scratch process of two grits with a Z-axis spacing of 0.5, 2.5, or 5 μm along the DOC direction were carried out. Figure 6 shows the top-view and middle cross-sectional images of damage distribution at the initial stage of interference in double scratching with the Δd_z of 0.5, 2.5, and 5 μm at different times separately. From Figure 6a, when t = 2.7 μs, very small surface cracks appeared in the scratching width direction and the direction was perpendicular to the scratching direction of the workpiece. Consequently, the material removal mode can be indexed as the combined plastic-brittle removal mode. As t = 3.0 μs, material damage interference occurred, and at the same time, because the Δd_z was relatively small, the material removal modes during double scratching were both combined plastic-brittle removal modes. After interference occurred, a relatively large population of radial cracks generated by the second grit appeared at the bottom of the groove, and at the end of the workpiece, the width and depth of material removal generated by the second grit were much larger than that generated by the first grit, which suggested that the subsurface damages induced by scratching were significantly intensified by the interference between themself.

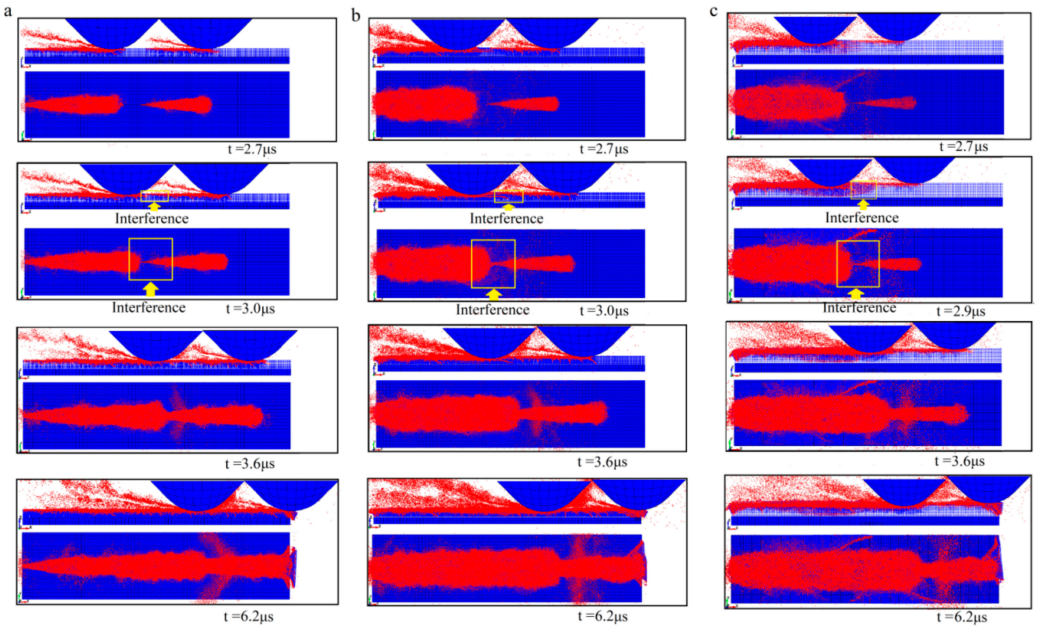

Figure 6. Damage interference nephograms of two grit scratching of single crystal SiC with a Z-axis spacing along the DOC direction at different times, (**a**) Δd_z is 0.5 μm, (**b**) Δd_z is 2.5 μm, and (**c**) Δd_z is 5 μm.

As can be seen from Figure 6b, when t = 2.7 μs, obvious lateral cracks generated by the first grit appeared at the bottom of the groove, and the width of the groove increased obviously. When the Δd_z was increased, the damage degree increased gradually. When t = 3.0 μs, the same interference moment as the case with the Δd_z = 0.5 μm, material damage interference occurred. At this moment, the material removal mode caused by the fist grit changes from plastic and brittle critical removal to a brittle removal, and the material removal mode caused by the second grit was still in a combined plastic-brittle removal mode. At t = 3.6 μs, the lateral cracks generated by the first grit interfered with the radial cracks generated by the second grit after multiple scratching, and the number and

length of lateral cracks and radial cracks increased significantly. After the occurrence of interference, material damage continued to escalate. Especially, damage in depth direction significantly intensified. Comparing with the scratching at the Δd_z of 0.5 μm, the width and depth of material removal generated by the second grit both increased. It also shows that the impact of the damage interference continues to increase in combined plastic-brittle removal mode with the increase of the DOC. Moreover, the effect of damage interference in the depth direction has priority over that of damage interference in the width direction.

Figure 6c shows that when the Δd_z is 5 μm, damage generated by the first scratching grit was further increased, i.e., changed from cracks to fragments. Moreover, the maximum width of the groove and the size of the cracks greatly increased. These results show that the material removal was complete in brittleness removal mode. When t = 2.9 μs, material damage interference occurs. Due to the formation of large fragments, the maximum width of the groove increased obviously, but the number of small cracks in the depth direction generated by the second grit decreased. However, due to the interference effect, material damage generated by the second grit was of a fragmentation feature and consequently, both the width and depth of the scratched groove obviously increased. It shows that when the depth difference changes from 2.5 microns to 5 microns, the material removal mode changes from combined plastic-brittle to brittle removal. In addition, the effect of damage interference in the width direction is far greater than that in the depth direction in the brittle removal mode.

4.2. Role of DOC

Figure 7a shows the variation of the *hin* and *bin* values in double scratching process with the Δd_z of 0.5, 2.5, 5, 15, and 25 μm. When the Δd_z was in the range of 0.5 to 5 μm, the *bin* and *hin* values increased gradually; when the Δd_z value was in the range of 5 to 25 μm, the *bin* and *hin* values suddenly decreased. This also shows that the interference effect first increases and then decreases. The interference effect in the depth direction was significantly greater than that in the width direction for the Δd_z of 0.5 μm and 2.5 μm. When the Δd_z was 5 μm, the interference effect in the depth direction was almost same as that along the width direction. However, for the Δd_z of 15 μm and 25 μm, the comparison was exactly the opposite. This indicates that although the *hin* and *bin* had the same trend with the Δd_z increasing, the strength of the interference in the width and depth direction with different Z-direction spacings were not consistent. Figure 7b shows the variation trends of interference time and internal energy of two grits scratching with the Δd_z of 0.5, 2.5, 5, 15 μm, and 25 μm. The interference time refers to the specific moment when the interference occurs, and internal energy is the sum of the energy required for all particles involved in motion. For the Δd_z of 0.5 μm and 2.5 μm, interference time was the same, and internal energy increased faster relatively. However for the Δd_z of 5, 15 μm, and 25 μm, the interference time was continuously advanced, and internal energy showed a linear trend; with the Δd_z increasing, and the internal energy gradually increasing.

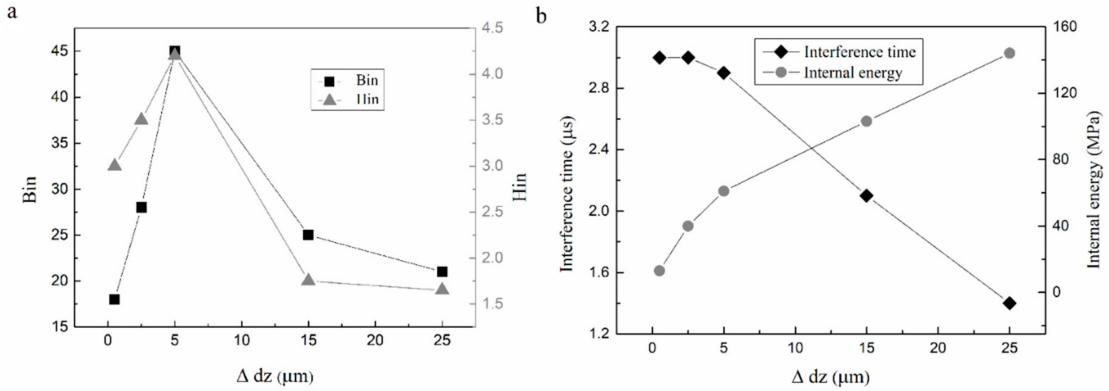

Figure 7. Other interference results of twice scratching with different Z-axis spacings along the DOC direction, (**a**) *Bin* and *Hin*, (**b**) and nterference time.

4.3. Interference Mechanisms

According to the above analysis, a comprehensive investigation on the damage interference were added at the microscale double scratching of single crystal SiC. When the Z-axis spacing along the DOC increases, the damage interference goes through the following three stages, as shown in Figure 8. The first stage (see Figure 8a) is when interference occurs, the material removal from the two grits is the same, both of which are the plastic-brittle coexistence removal. Damage forms are mainly plastic slip and micro cracks. Interference enhances the material removal, and the interference effect in the depth direction is significantly larger than that in the width direction relatively. The second stage (see Figure 8b) is where material removal generated by the first grit changed into brittle removal. Damage in this stage is dominated by muti-propagating cracks and little fragments. Though the material removal generated by the two grits is different, the dominant modes are both brittle removal modes. Compared to the previous stage, interference continues to be enhanced, especially in the width direction, and the interference effect in the depth direction is consistent with that in the width direction basically. The second stage is the strongest stage of interference. The third stage (see Figure 8c), is when the material removal generated by the first grit is completely in the brittle removal mode and the material removal generated by the second grit is still in the plastic-brittle coexistence mode, and owing to the intersection of cracks, materials crumbles in fragments quickly. Damage in this stage is dominated by large fragments; although, the main forms of material damage do not change, the larger the Z-axis spacing between the two grits along the DOC direction, the weaker the interference. With the increase of the Z-axis spacing along the DOC direction, the influence of interference on material removal depth decreases gradually, which is less than the effect of the increased scratch depth.

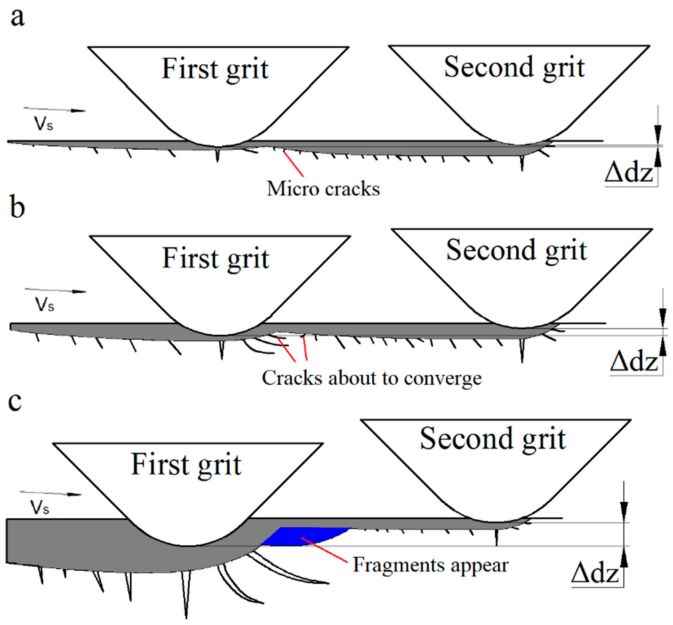

Figure 8. Material damage interference forms in micron scale with different Z-axis spacings along the DOC direction, (**a**) the first stage, (**b**) the second stage, and (**c**) the third stage.

5. Conclusions

In this paper, the damage interference mechanisms during double scratching of single crystal SiC with different Z-axis spacing along the DOC direction was analyzed using the FE/SPH coupled numerical simulation algorithm, which was also validated through the double scratching experiments. Based on both experimental result and numerical analysis, the following conclusions can be drawn:

1. At micron scales, damage interference can be divided into three stages according to the DOCs: a combined plastic-brittle interference enhancement stage when DOC was less than 5 μm, a crack

interference stage as DOC was increased to 5 μm, and a weakened interference stage when fragmentation occurred.

2. When the Z-axis spacing along the DOC direction was small and material removal mode was in combined brittle-plastic mode, the interference was mainly in the depth direction. As the Z-axis spacing increased to initiate the brittleness removal of SiC, the scratching damage was mostly interfered in the width direction.
3. Initiation time of damage interference was also related to the materials removal modes at variable DOCs, and when SiC was removal completely in the brittle mode, the damage interference was triggered earlier than that in a combined brittle-plastic removal mode.

Funding: This research was supported by the National Youth Foundation of China (Grant No. 51805175) and by the National Natural Science Foundation of China (Grant No. 51575197).

Conflicts of Interest: The author declare no conflict interests. The funders had no role in the design of the study; in the collection, analyses, or interpretation of data; in the writing of the manuscript, or in the decision to publish the results.

References

1. Casady, J.B.; Johnson, R.W. Status of silicon carbide (SiC) as a wide-band gap semiconductor for high-temperature applications. *Solid State Electron.* **1996**, *39*, 1409–1422. [CrossRef]
2. Hobgooda, H.M.; Bradya, M.; Brixius, W. Growth and Characterization of Semiconductor Silicon Carbide for Electronic and Optoelectronic Applications: An Industrial PersPeetive. Ph.D. Thesis, Hiroshima University, Higashihiroshima, Japan, 2001.
3. Maksakova, O.V.; Simoēs, S.; Pogrebnjak, A.D.; Bondar, O.V.; Kravchenko, Y.O.; Koltunowicz, T.N.; Shaimardanov, Z.K. Experimental and theoretical studies of the physicochemical and mechanical properties of multi-layered TiN/SiC films: Temperature effects on the nanocomposite structure. *Compos. Part B-Eng.* **2018**, *142B*, 85–94.
4. Liu, B.; Yu, Y.; Tang, X.; Gao, B. Improvement of Growth Interface Stability for 4-Inch Silicon Carbide Crystal Growth in TSSG. *Crystals* **2019**, *9*, 653. [CrossRef]
5. Levinshtein, M.E.; Rumyantsev, S.L.; Shur, M.S. *Properties of Advanced Semiconductor Materials: GaN, AlN, InN, BN, SiC, SiGe*; Wiley& Sons, Inc.: New York, NY, USA, 2001.
6. Liao, X.J.; Mu, D.K.; Fu, W.; Huang, H.; Huang, H. Low-temperature wetting mechanisms of polycrystalline chemical vapour deposition (CVD) diamond by Sn-Ti solder alloys. *Mater. Design.* **2019**, *182*, 108039. [CrossRef]
7. Maksakova, O.V.; Webster, R.F.; Tilley, R.D.; Ivashchenko, V.I.; Postolnyi, B.O.; Bondar, O.V.; Takeda, Y.; Rogoz, V.M.; Sakenova, R.E.; Zukowski, P.V.; et al. Nanoscale architecture of (CrN/ZrN)/(Cr/Zr) nanocomposite coatings: Microstructure, composition, mechanical properties and first-principles calculations. *J. Alloy. Compd.* **2020**, *831*, 154808. [CrossRef]
8. Murahara, M.M. Excimer-laser-induced photochemical polishing of SiC mirror. *Proc. SPIE.* **2002**, *4679*, 69–74.
9. Chen, X.F.; Xu, X.G.; Hu, X.B. Anisotropy of Chemical Mechanical Polishing in Silicon Carbide Substrates. *Mat. Sci. Eng. B-Solid.* **2007**, *142*, 28–30. [CrossRef]
10. Zhu, D.H.; Yan, S.J.; Li, B.Z. Single-grit modeling and simulation of crack initiation and propagation in SiC grinding using maximum undeformed chip thickness. *Comp. Mater. Sci.* **2014**, *92*, 13–21. [CrossRef]
11. Petit, F.; Ott, C.; Cambier, F. Multiple scratch tests and surface-related fatigue properties of monolithic ceramics and soda lime glass. *J. Eur. Ceram. Soc.* **2009**, *29*, 1299–1307. [CrossRef]
12. Gu, W.B.; Yao, Z.Q.; Liang, X.G. Material removal of optical glass BK7 during single and double scratch tests. *Wear* **2011**, *270*, 241–246. [CrossRef]
13. Klecka, M.; Subhash, G. Grain size dependence of scratch-induced damage in alumina ceramics. *Wear* **2008**, *265*, 612–619. [CrossRef]
14. Li, C.; Zhang, F.H.; Wang, X.; Rao, X.S. Repeated nano scratch and double nano scratch tests of Lu2O3 transparent ceramics: Material removal and deformation mechanism, and theoretical model of penetration depth. *J. Eur. Ceram. Soc.* **2018**, *38*, 705–718. [CrossRef]

15. Zhang, P.; Zhao, H.W.; Shi, C.L.; Zhang, L.; Huang, H.; Ren, L.Q. Influence of double-tip scratch and single-tip scratch on nano-scratching process via molecular dynamics simulation. *Appl. Surf. Sci.* **2013**, *280*, 751–756. [CrossRef]
16. Benz, W.; Asphaug, E. Simulations of brittle solids using Smoothed Particle Hydrodynamics. *Comput. Phys. Commun.* **1995**, *87*, 253–265. [CrossRef]
17. Sauer, M. Adaptive, Kopplung des Netzfreien SPH-Verfahrens mit Finiten Elementen zur Berechnung von Impaktvorgangen. Ph.D. Thesis, Universitat der Bundeswehr Miinchen, Neubiberg, Germany, 2000.
18. Limido, J.; Espinosa, C.; Salaun, M.; Lacome, J.L. SPH method applied to high speed cutting modeling. *Int. J. Mech. Sci.* **2007**, *49*, 898–908. [CrossRef]
19. Grimaldi, A.; Sollo, A.; Guida, M.; Marulo, F. Parametric study of a SPH high velocity impact analysis-A birdstrike windshield application. *Compos. Struct.* **2013**, *96*, 616–630. [CrossRef]
20. Lin, J.; Naceur, H.; Coutellier, D.; Laksimi, A. Efficient meshless SPH method for the numerical modeling of thick shell structures undergoing large deformations. *Int. J. Nonlin. Mech.* **2014**, *65*, 1–13. [CrossRef]
21. Mahnama, M.; Movahhedy, M.R. Application of FEM simulation of chip formation to stability analysis in orthogonal cutting process. *J. Manuf. Process.* **2012**, *14*, 188–194. [CrossRef]
22. Han, L.; Zhang, Y.; Li, X.-M.; Jiang, L.-H.; Chen, D. Accelerated Approach for the Band Structures Calculation of Phononic Crystals by Finite Element Method. *Crystals* **2016**, *6*, 11. [CrossRef]
23. Wang, Y.; Cao, M.; Zhao, X.R.; Zhu, G.; McClean, C.; Zhao, Y.Y.; Fan, Y.B. Experimental investigations and finite element simulation of cutting heat in vibrational and conventional drilling of cortical bone. *Med. Eng. Phys.* **2014**, *36*, 1408–1415. [CrossRef]
24. Wang, H.; Lu, C.; Tieu, K. A Combined Experiment and Crystal Plasticity FEM Study of Microstructure and Texture in Aluminium Processed by Reverse and Unidirectional Accumulative Roll-Bonding. *Crystals* **2019**, *9*, 119. [CrossRef]
25. Wu, H.B.; To, S. Serrated chip formation and their adiabatic analysis by using the constitutive model of titanium alloy in high speed cutting. *J. Alloy. Compd.* **2015**, *629*, 368–373. [CrossRef]
26. Cao, J.; Wu, Y.; Li, J.; Zhang, Q. Study on the material removal process in ultrasonic-assisted grinding of SiC ceramics using smooth particle hydrodynamic (SPH) method. *Int. J. Adv. Manuf. Tech.* **2016**, *83*, 985–994. [CrossRef]
27. Duan, N.; Yu, Y.Q.; Wang, W.S.; Xu, X.P. SPH and FE Coupled 3D Simulation of Monocrystal SiC Scratching by Single Diamond Grit. *Int. J. Refract. Met. Hard Mater.* **2017**, *64*, 279–293. [CrossRef]
28. Duan, N.; Yu, Y.Q.; Wang, W.S.; Xu, X.P. Analysis of Grit Interference Mechanisms for the Double Scratching of Monocrystalline Silicon Carbide by Coupling the FEM and SPH. *Int. J. Mach. Tool. Manu.* **2017**, *120*, 49–60. [CrossRef]
29. Duan, N.; Huang, S.G.; Yu, Y.Q.; Huang, H.; Xu, X.P. The Influence of Brittle-Ductile Transition of Monocrystal SiC Scratching by Single Diamond Grit with Different Tip Radius. *Chin. J. Mech. Eng-en.* **2017**, *15*, 185–194.
30. Malkin, S.; Guo, C. Grinding technology: Theory and applications of machining with abrasives. *Int. J. Mach. Tool. Manu.* **1991**, *31*, 435–436.
31. Holmquist, T.J.; Templeto, D.W.; Bishnoi, K.D. Constitutive Modeling of Aluminum Nitride for Large Strain, High-strain Rate, and High-pressure Aplications. *Int. J. Impact. Eng.* **2001**, *25*, 211–231. [CrossRef]